



Efficient electrocatalytic desulfurization and synchronous hydrogen evolution from H₂S via anti-sulfuretted NiSe nanowire array catalyst

Chao Duan ^{a,b}, Chun Tang ^{b,*}, Shan Yu ^b, Lina Li ^c, Jinjin Li ^d, Ying Zhou ^{a,b,**}

^a State Key Laboratory of Oil and Gas Reservoir Geology and Exploitation, Southwest Petroleum University Chengdu, 610500, China

^b School of New Energy and Materials, Southwest Petroleum University Chengdu, 610500, China

^c Shanghai Synchrotron Radiation Facility, Shanghai Institute of Applied Physics, Chinese Academy of Sciences, Shanghai 201204, China

^d Laboratory of Natural Gas Sweetening, Research Institute of Natural Gas Technology, PetroChina Southwest Oil & Gas Field Company, Chengdu 610213, Sichuan, China



ARTICLE INFO

Keywords:

Electrocatalysis

Hydrogen evolution

Sulfur oxidation reaction

HER coupling reaction

ABSTRACT

Decreasing energy consumption of water splitting strategy by replacing oxygen evolution reaction (OER) with more facile sulfide oxidation reaction (SOR) to H₂ evolution and value-added sulfur products is a promising technology. Nevertheless, the unsatisfactory catalyst long-term stability and passivation issues substantially limit the overall productivity. Herein, we report an anti-sulfuretted NiSe nanowire array catalyst on nickel foam (NiSe/NF), this catalyst exhibits a significantly reduced anode potential of 0.49 V vs. RHE at 100 mA cm⁻² compared to the oxygen evolution reaction (1.78 V vs. RHE) and remains admirable stability for more than 500 h without passivation. Particularly, the skillful combination of UV-vis, *in situ* Raman, and attenuated total reflection Fourier transform infrared spectra, we reveal that S²⁻/HS⁻ has been selectively converted to S_n²⁻ and by-product S₂O₃²⁻ rather than sulfur, which avoids long-perplexing passivation issue of solid sulfur. For the first time, we demonstrate the feasibility of the system (SOR + HER) in a commercial membrane electrode assembly stack, which affords 19.0 mL min⁻¹ H₂ at a low cell voltage of 1.0 V with consuming the electricity of 2.63 kWh Nm⁻³ H₂. This work provides a new avenue for low-cost H₂ production by H₂S electrooxidation desulfurization.

1. Introduction

Electrocatalytic water splitting powered by clean energy to produce green H₂ is considered a promising alternative strategy because of the limited source of fossil fuels and increasing environmental contamination [1,2]. However, the oxygen evolution reaction (OER) still sustains huge overall electricity consumption due to the sluggish process for the multiple proton and electron transfer steps [3]. Replacing the OER with a thermodynamically more readily oxidation reaction to reduce overall energy consumption is a potentially energy-saving approach to facilitate H₂ production. Besides, the anode oxidation reactions have the extra advantage of obtaining valuable chemicals or dealing with environmental pollution, such as electrooxidation of alcohols, hydrazine, 5-hydroxymethylfurfural, wastewater, and waste gas *et. al*[4–6].

In the above electrooxidation reactions, the H₂S oxidation degradation has received wide attention because of 10 million tons of emissions per year from sour natural gas and ultra-low oxidation potential (0.17 V)

compared with oxygen evolution reaction (1.23 V) [7–9]. With extreme toxicity and corrosivity, H₂S has to be pretreated for further exploitation of high sulfur gas reservoirs. The conventional method for H₂S purification relies on the Claus process (H₂S + 3/2 O₂ → SO₂ + H₂O, 2 H₂S + SO₂ → 2 H₂O + 3 S, > 1000 °C), through which only sulfur is recycled, while H₂ is wasted and SO₂ unavoidably emitted [10]. Therefore, the electrocatalytic degradation of H₂S is a promising energy conversion technology for simultaneously energy-saving H₂ production and sulfur recovery under mild conditions. However, this one-stone-kills-two birds technology is limited by unexpected anodic sulfur passivation and poisoning effect in a sulfur-rich environment, which substantially decreases electrocatalytic activity and long-term stability [11].

To resolve sulfur passivation, indirect routes were developed involving redox mediators (Fe²⁺/Fe³⁺, VO²⁺/VO²⁺, I⁻/I₃⁻) to oxidize S²⁻ anions, which are restricted by complicated process [12–17]. Alternatively, direct routes have been developed to alleviate sulfur passivation including the mechanical stirring method, sulfur dissolution with

* Corresponding author.

** Corresponding author at: State Key Laboratory of Oil and Gas Reservoir Geology and Exploitation, Southwest Petroleum University Chengdu, 610500, China.

E-mail addresses: tangchun@swpu.edu.cn (C. Tang), yzhou@swpu.edu.cn (Y. Zhou).

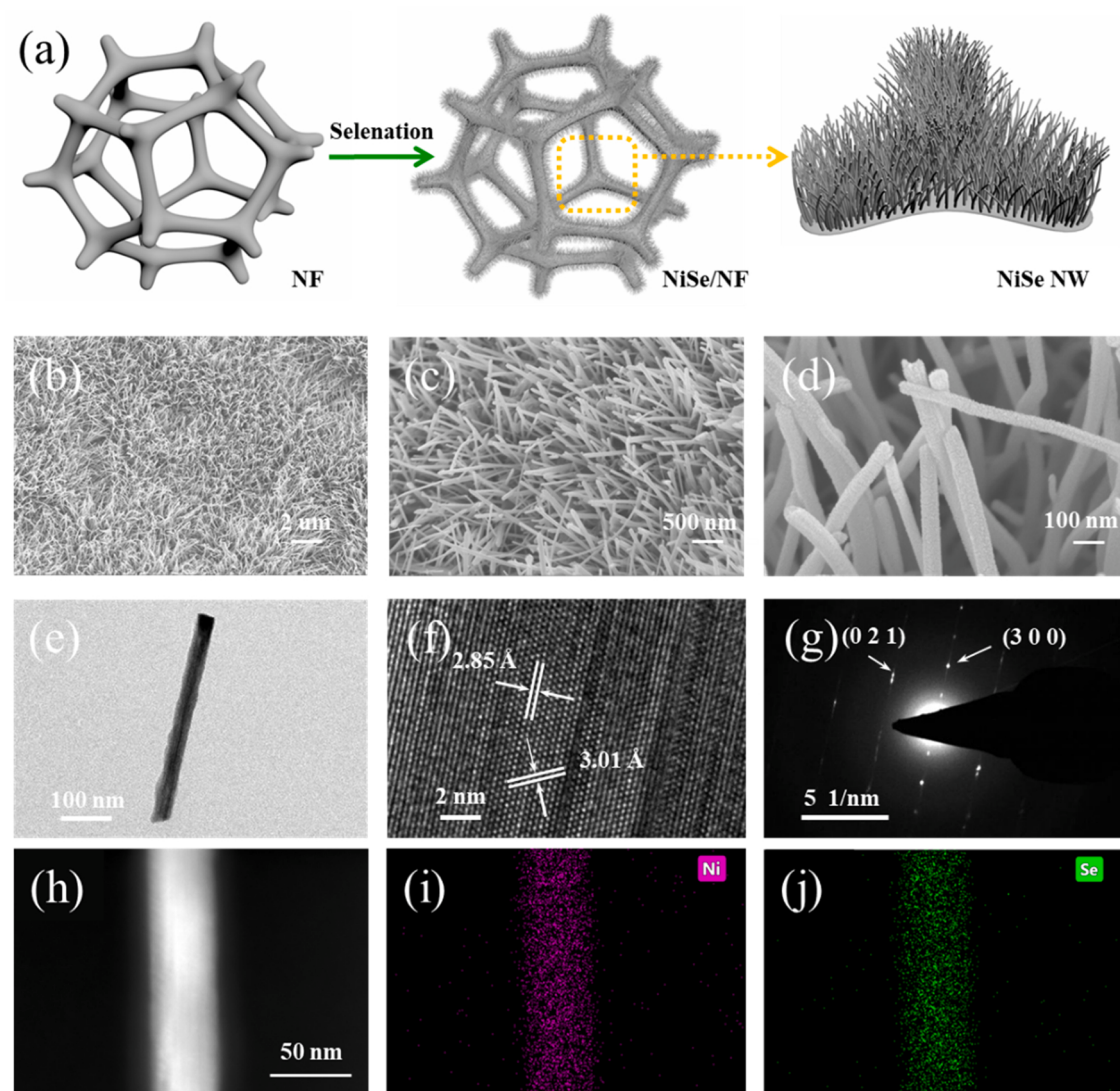


Fig. 1. (a) Schematic diagram of the *in situ* grown process for preparing NiSe/NF catalysts; (b-d) SEM images of NiSe/NF; (e) TEM image of one NiSe nanowire; (f) HRTEM image and (g) SAED pattern of NiSe nanowire; (h-j) HAADF-STEM image and EDX elemental mapping of Ni and Se for NiSe nanowire.

organic solvents, and sulfur sublimation [18–20], which need extra toxic organics or consume tremendous energy. Recently, Deng et al. developed chainmail catalysts to avoid sulfur poison and hence achieved a relatively stable performance [21,22]; Zhang et al. reported self-cleaning electrodes to weaken interaction with sulfur species [23]. Despite impressive progress in electrocatalysts for H₂S splitting [24–27], the investigation of sulfide oxidation reaction (SOR) mechanisms is still in its infancy, which also strongly affects the H₂ evolution performance. Particularly, according to the potential-pH diagrams [28], elemental sulfur, S_n²⁻, and various oxyanions such as SO₃²⁻, S₂O₃²⁻, SO₄²⁻ et al. are involved in the oxidation of sulfide solutions [29], and these oxyanions undoubtedly affect the long-term stability of H₂ production. However, revealing the mechanism of H₂S oxidation to realize further sustainable H₂ production has been rarely explored.

In previous reports, selenides show good stability in sulfur-containing solutions [30–32]. Besides, NiSe has good conductivity and excellent activity, which is widely used in lithium-sulfur batteries and water electrolysis [33–35]. Herein, we develop an anti-sulfuretted integrated NiSe nanowire array on Ni foam (NiSe/NF) for efficient electrocatalytic desulfurization coupling energy-saving H₂ production. Notably, the NiSe/NF exhibits unprecedented performance in alkaline media compared with precious Pt/C and RuO₂ catalysts, displaying 500 h durability with no decay at 0.4 V. Particularly, by combining UV-vis,

in situ Raman, and attenuated total reflection Fourier transform infrared (ATR-FTIR) spectra, we reveal that the efficient H₂S electrooxidation degradation of NiSe/NF originates from the S²⁻ and HS⁻ mostly converted to S_n²⁻ and by-product S₂O₃²⁻ rather than sulfur in solution. Our results are essential to understand the intrinsic SOR mechanism and further regulate the product selectivity.

2. Experimental

2.1. Materials

NF was purchased from Kunshan Long Sheng Bao electronic material, NaBH₄ and Se powder were bought from Chengdu Chron Chemicals Co. Ltd., and Hydrochloric acid (HCl) and ethanol were purchased from Aladdin Ltd. (Shanghai, China). All the reagents were used as received. The water used throughout all experiments was purified through a Millipore system.

2.2. Preparation of NiSe/NF catalyst

A piece of NF ($2 \times 3 \text{ cm}^2$) was washed with 3 M HCl, ethanol, and deionized water several times to ensure the surface of the NF was well cleaned before use. For the preparation of NaHSe solution, 0.118 g Se

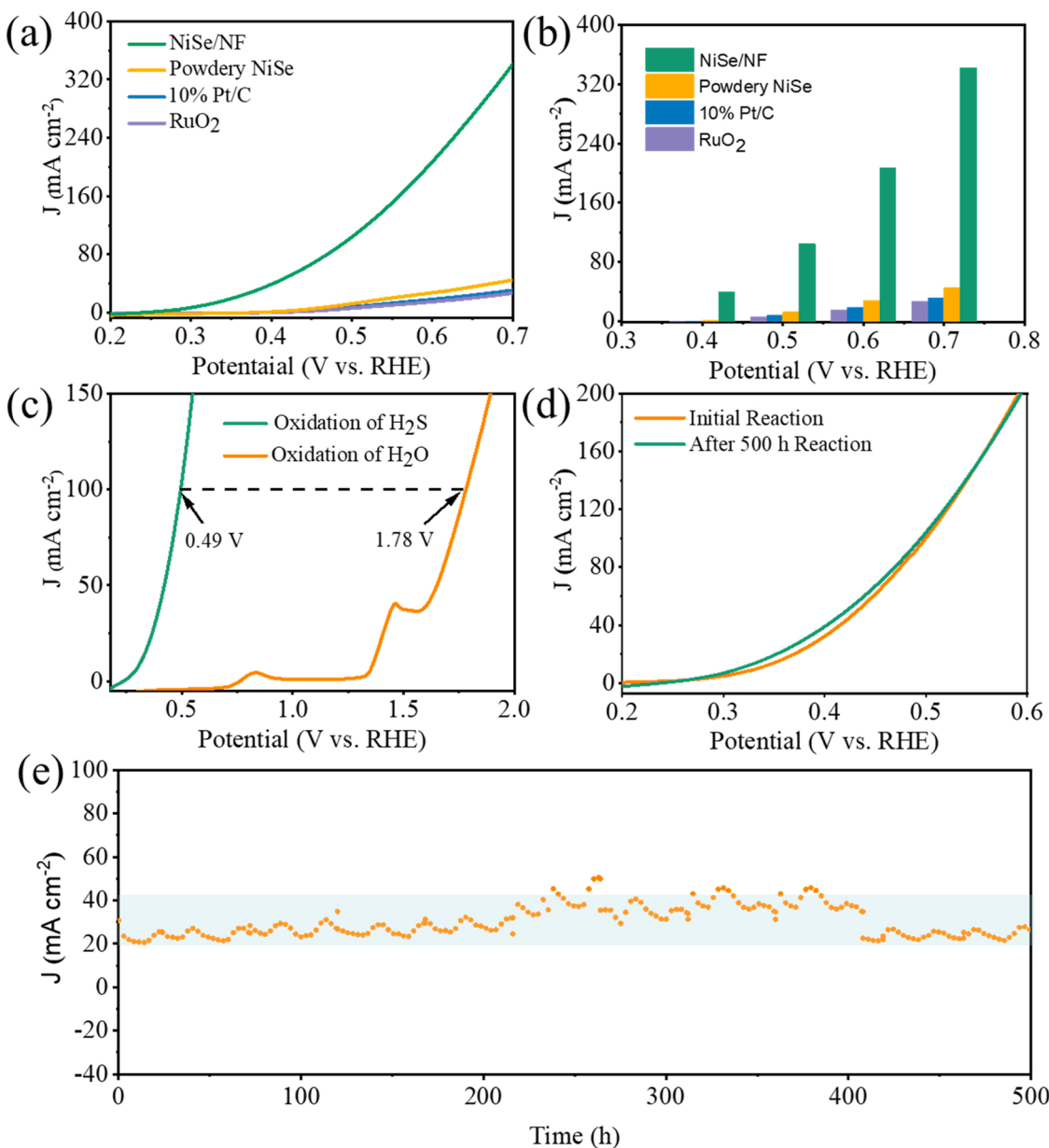


Fig. 2. (a) SOR polarization curves of NiSe/NF in comparison with other catalysts. (b) Current densities for NiSe/NF, powdery NiSe, 10 % Pt/C, and RuO₂ at the potential of 0.4–0.7 V for SOR. (c) Comparison of the LSV curves between the SOR and OER on the NiSe/NF electrode. (d) The LSV of NiSe/NF before and after 500 h stability test for SOR. (e) Durability measurement of NiSe/NF at 0.4 V for 500 h.

powder was added into 3 mL deionized water containing 0.130 g NaBH₄. After gently stirring for several minutes, a clear NaHSe solution was obtained. The freshly prepared NaHSe solution was added to 30 mL ethanol under N₂ flow. Then the solution was transferred into a 50 mL Teflon-lined stainless steel autoclave with a piece of pretreated NF maintained at 140 °C for 12 h in an electric oven. After the autoclave cooled down slowly at room temperature, the sample was collected and washed with water and ethanol several times and then dried at 60 °C for 4 h. The mass of NiSe catalyst on NF was calculated as follows. The weight increment (x mg) of NF can be directly weighted after the growth of NiSe. $\text{NiSe}_{\text{loading}} = x \text{ mg} \times (M_{\text{NiSe}}/M_{\text{Se}}) = x \text{ mg} \times (138/79) = 1.747 \times \text{mg}$, where M is the molecular weight or atomic weight. For NiSe/NF electrode, the loading mass of NiSe is about 7.8 mg cm⁻².

2.3. Characterizations

XRD data were acquired on a Philips X'Pert diffractometer with Cu

K α radiation ($\lambda = 1.5418 \text{ \AA}$). SEM measurements were carried out on a ZEISS Sigma 300 scanning electron microscope at an accelerating voltage of 20 kV. TEM measurements were performed on FEI TECNAI G20 electron microscopy (FEI, American) with an accelerating voltage of 200 kV. Energy dispersive spectroscopy (EDS) mapping were conducted by FEI TF20. XPS measurements were performed on a Thermo Fisher Scientific K-Alpha X-ray photoelectron spectrometer using Mg as the exciting source. The ATR-FTIR measurements were carried out on a Bruker infrared spectrometer (Tensor II) equipped with a liquid nitrogen-cooled mercury-cadmium-telluride (MCT) detector. The *in situ* Raman spectra were performed by a high-resolution Raman spectrometer system (Horiba LabRam HR) equipped with 473 nm laser excitations.

2.4. Electrochemical measurements

Electrochemical measurements were performed with a CHI 660D

electrochemical analyzer (CH660 Instruments, Inc., Shanghai) in a standard three-electrode system using NiSe/NF as the working electrode, a graphite rod as the counter electrode and a Hg/HgO electrode as the reference electrode. All potentials measured were calibrated to RHE using the following equation: $E(\text{RHE}) = E(\text{Hg/HgO}) + 0.098 \text{ V} + 0.0591 * \text{pH}$. Polarization curves were obtained using LSV with a scan rate of 5 mV s^{-1} and no activation was used before recording the polarization curves. The long-term durability test was performed using chronoamperometry measurements. To weaken the influence of reactant concentration on catalyst activity, the electrolyte was replaced every 6 days.

3. Results and discussion

3.1. Synthesis and characterization

Fig. 1a exhibits the synthesis procedure of integrated NiSe/NF by direct selenization of commercially available Ni foam. The crystal structure of NiSe/NF was characterized by x-ray diffraction (XRD). **Fig. S1** shows the peaks belonging to NiSe (PDF No.18-0887) [36,37]. Moreover, the surface morphologies of NiSe/NF were reflected by Scanning electron microscope (SEM) and transmission electron microscopy (TEM) images, and the NiSe nanowire array was observed in **Fig. 1b-e**. High-resolution TEM (HRTEM) with the results shown in **Fig. 1f**, the interplanar distances of 2.85 and 3.01 \AA can be identified as (300) and (101) planes of NiSe (**Fig. 1f**), respectively. The selected-area electron-diffraction (SAED) pattern (**Fig. 1g**) displays discrete spots corresponding to the (300), (021) planes of the NiSe. The HAADF-TEM and EDS mapping images further reveal the uniform distribution of Se and Ni (**Fig. 1h-j**). X-ray photoelectron spectroscopy (XPS) in **Fig. S2** offers the valence state of NiSe. Meanwhile, in the Fourier-transformed (FT) k^3 -weighted extended X-ray absorption fine structure (EXAFS) spectra (**Fig. S3**), the peak at about 2.08 \AA is assigned to the Ni-Se scattering path [38]. Thus, we can conclude that the NiSe nanowire array is successfully grown on Ni foam.

3.2. Electrocatalytic performance

The electrocatalytic performances for SOR were evaluated in 1.0 M NaOH solution with or without $1.0 \text{ M Na}_2\text{S}$. Linear sweep voltammograms (LSVs) over various catalysts were determined. As shown in **Fig. 2a**, Pt/C, RuO₂, and powdery NiSe exhibit very limited activity with the need potential of around 0.5 V to drive 10 mA cm^{-2} . Remarkably, NiSe/NF electrode presents greatly enhanced SOR activity and it only demands a low potential of 0.14 V to drive the same current density. In sharp contrast, NiSe/NF exhibits a negligible current density in 1.0 M NaOH solution under the same potential window (**Fig. S4**). Furthermore, the current density of integrated NiSe/NF at 0.7 V is 7.6 times of powdery NiSe owing to the electron highway between the catalyst and substrate (**Fig. 2b**). Compared with the potential for OER of electrocatalytic water splitting, the SOR potential of NiSe/NF at 100 mA cm^{-2} is only 0.49 V , which is 1.29 V lower than that of OER (**Fig. 2c**). Besides, we also explored the cathodic HER activity of NiSe/NF as shown in **Fig. S5a**. LSV curves for HER indicate that NiSe/NF has better electrocatalytic activity than nickel foam and Pt foil. For HER coupled SOR system, H_2 is a rapidly produced at significantly lower potential, which indicate that SOR is more favorable than OER to promote hydrogen evolution (**Fig. S5b**). Moreover, a comparison of SOR with reported water electrolyzers coupling HER and various anodic reactions was summarized in **Table S1**, the potential at current density for 100 mA cm^{-2} of various anodic reactions sharply demonstrate that SOR is more conducive to occurring at a low potential.

To understand the enhanced SOR performance, the electrochemical active surface area (ECSA) of NiSe/NF and NF was estimated from the electrochemical double-layer capacitance (**Fig. S6**) [39]. The capacitance of NiSe/NF and NF is 10.89 mF cm^{-2} and 0.27 mF cm^{-2} ,

Table 1

The performance and durability of SOR for NiSe/NF compared with the previous works.

Catalysts	Current density (mA cm^{-2})	Stability (h)	Activity at 0.6 V (mA cm^{-2})	Ref.
NiSe/NF	~ 30	500	~ 207	This work
CoNi@NGs	~ 25	500	~ 150	[21]
Ni ₃ S ₂	~ 20	100	~ 80	[23]
WS ₂	~ 70	192	~ 58	[24]
CuS/NF	~ 50	48	~ 200	[25]
CoFeS ₂	~ 50	120	~ 200	[26]
CoS ₂ @C/MXene/NF	~ 300	240	~ 250	[27]
Co-Ni ₃ S ₂	/	24	~ 100	[48]
Ni ₃ S ₂	/	/	~ 80	[48]
NiCu-MoS ₂	75	150	~ 290	[49]
MoS ₂	/	/	~ 100	[49]
Ni-MoS ₂	/	/	~ 180	[49]
Cu-MoS ₂	/	/	~ 150	[49]

respectively, indicating NiSe/NF further steers the kinetics of SOR by producing more catalytic active sites. On the other hand, electrochemical impedance spectroscopy (EIS) is a significant test method in studying the kinetics process. **Fig. S7** illustrates the Nyquist plots of the measured impedance of the SOR process on NiSe/NF and NF electrodes from an open circuit potential (OCP) to 0.507 V . These Nyquist plots were fitted with an equivalent circuit. The R_{ct} and CPE represent the S^* ions adsorption resistance and pseudocapacitance, respectively [40]. The changing trend of R_{ct} and CPE could reveal the S^* evolution on the catalyst surface during SOR. Similar studies have been reported for $\text{H}\bullet$ and $\text{OH}\bullet$ evolution in the HER and OER processes, respectively [41]. NiSe/NF electrode at different potential presents similar R_s values, the changes of total charge transfer resistance is dominated by R_{ct} with the adsorbed S^* intermediate species during SOR. As shown in **Table S2**, NiSe/NF catalyst possesses lower R_{ct} that suggests fast charge-transfer kinetics, confirming the superior catalytic activity.

Stability is a crucial parameter to evaluate the long-term SOR of the electrocatalysts for practical applications. In previous reports, Pt, Ni foil, and metal oxides were easily passivated and poisoned [23]. Deng et al. reported graphene-encapsulated CoNi alloy (CoNi@NGs) to protect the catalyst active center from sulfide passivation and poisoning. In addition, a series of metal sulfides also have good sulfur resistance for SOR.

Table 1 compares the durability and current density with reported catalysts. Among the listed catalysts, the CoNi@NGs catalyst exhibited relatively well activity and stability, but the synthesis process of chainmail catalysts is complex and expensive. Interestingly, NiSe/NF with nano brush structure has similar properties to metal sulfides, which also exhibited excellent anti-sulfurated stability without any protection strategy. As expected, the polarization curve after the 500 h durability test shows a high performance without decay compared with the initial (**Fig. 2d**). As shown in **Fig. 2e**, the long-term electrochemical stability of NiSe/NF was also examined by chronopotentiometry at a constant potential of 0.4 V for 500 h , the current density of NiSe/NF remained at around 30 mA cm^{-2} . The fluctuations of stability are due to temperature differences between day and night according to **Fig. S8**. Moreover, the XRD, XPS, TEM, SEM and EDS characterization of NiSe/NF after stability test are given in **Fig. S9**. The XRD, SEM and TEM images indicate that catalyst remains NiSe crystal structure and nanowire morphology (**Fig. S9a,d,e**). The Ni 2p XPS analysis after reaction rules out the formation of oxyhydroxide or oxide species on NiSe surface due to far lower anodic potential of SOR than that of OER in sulfion solution (**Fig. S9b-c**). Meanwhile, it still can be clearly seen that the existence of Ni, Se elements in NiSe/NF after SOR (**Fig. S9f**), we logically consider the actual active specie is probably still NiSe phase. Therefore, the extremely high stability of NiSe/NF prompts us to further explore the SOR mechanism.

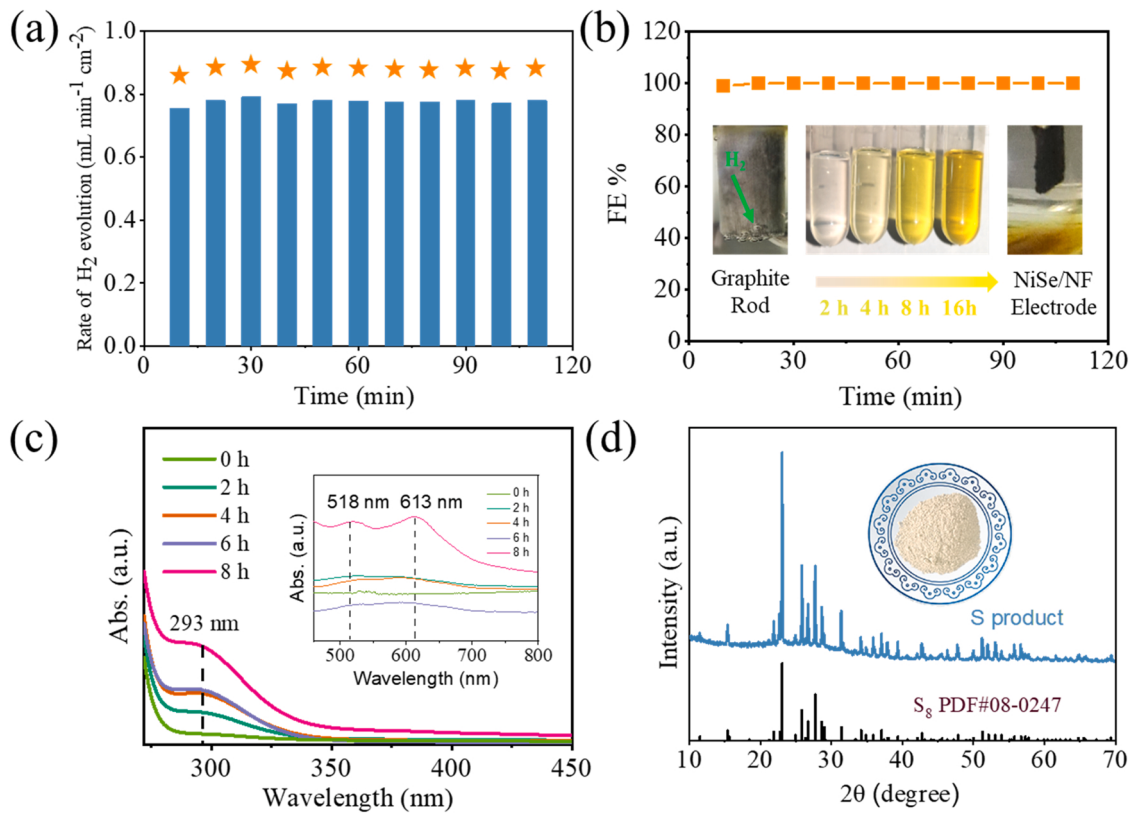


Fig. 3. (a) H₂ production rates and (b) H₂ Faradaic efficiencies in galvanostatic test at 100 mA cm⁻² (inset: photograph with the reaction procedure); (c) UV-Vis spectra of 100 times diluted electrolyte at different times; (d) XRD spectra of the anodic product after acidification (inset: photograph of the collected product of S powder).

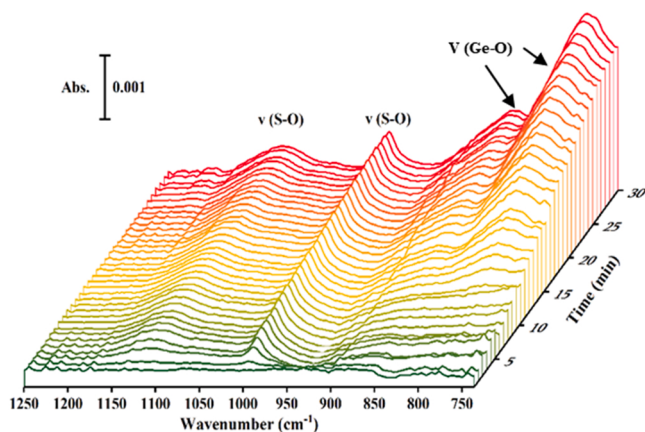


Fig. 4. In situ ATR-FTIR spectra during a chronoamperometry test at 0.627 V on the NiSe/NF electrode in 1.0 M Na₂S and NaOH solution.

3.3. Mechanism investigation

To clarify the anode and cathodic actual products, we carry out a galvanostatic test at 100 mA cm⁻² current density, the cathode gas was identified as H₂ by gas chromatograph with H₂ production rate remained at around 0.77 mL min⁻¹ cm⁻² which extrapolates 99.9 % H₂ faradaic efficiency (Fig. 3a, b). As the reaction proceeds, the anodic electrolyte becomes yellow and darker (inset of Fig. 3b), which implies an increase the concentration of S_n²⁻ [42,43].

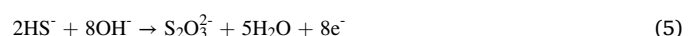
To investigate the mechanism of SOR, we firstly used UV-vis to probe the products in the electrolyte. Fig. 3c reveals the peaks shown at 297 nm, 518 nm, and 613 nm, corresponding to the chain polysulfides

(S₂²⁻-S_n²⁻) in the electrolyte [29,44],

and the signal strength of the polysulfides increases obviously as the reaction progresses. In addition, anodic yellow powder product after acidification (Fig. 3d), corresponded to elemental sulfur by XRD characterization [45]. Therefore, the reaction equations of SOR in the solution can be expressed as the following Eqs. (1)–(3):



Besides, we designed *in situ* electrochemical ATR-FTIR spectroscopy systems to evaluate the sulfide oxidative products in the electrolyte (Fig. S10a). To identify the wavenumber of sulfur-related species peaks, ATR-FTIR tests for a series of sulfur-related electrolytes are conducted (Fig. S11). Table S3 lists the characteristic peaks of SO₃²⁻ (935 cm⁻¹), S₂O₃²⁻ (997 cm⁻¹, 1115 cm⁻¹), SO₄²⁻ (1099 cm⁻¹), according to Fig. S11 and previous works [29]. Fig. 4 exhibits *in situ* electrochemical ATR-FTIR spectroscopy. With the development of anodic oxidation at 0.627 V, the peak at 1117 cm⁻¹, and 997 cm⁻¹ corresponding to the S-O stretching vibration of S₂O₃²⁻ increases with time, which indicates that S²⁻/HS⁻ can be oxidized to S₂O₃²⁻ in alkaline conditions. Furthermore, the FTIR spectroscopy without NiSe/NF catalyst as blank experiment was studied. As presented in Fig. S12, the two peaks around 750–850 cm⁻¹ wavenumber likely assign to Ge-O bond vibration of germanium crystal exclude sulfur-related species according to previous work reported [56]. Thus, the pathway is derived as the following Eqs. (4)–(5):



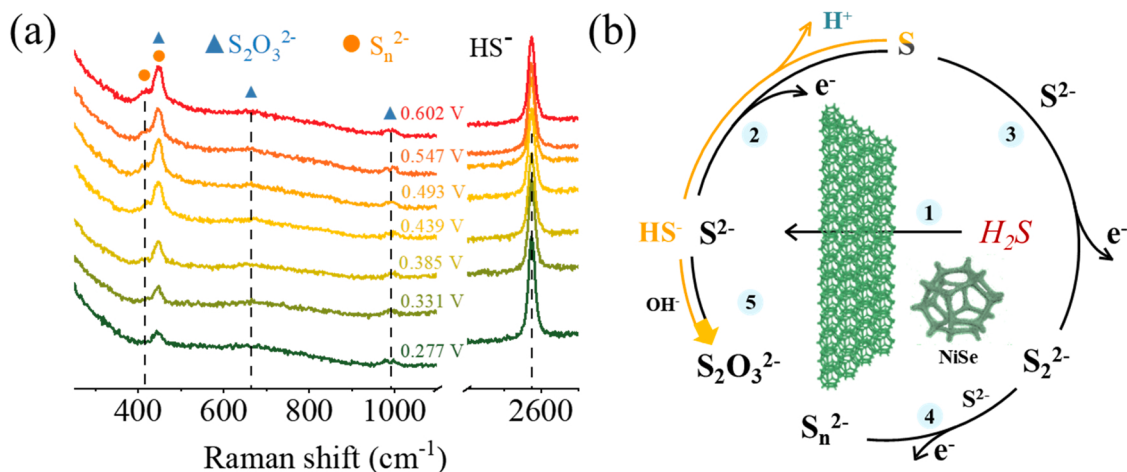


Fig. 5. (a) In situ Raman spectra in the range of 250–2800 cm⁻¹ at a potential between 0.277 and 0.602 V on NiSe/NF electrode in 1.0 M Na₂S and NaOH solution; (b) Illustration of SOR reaction routes over NiSe/NF.

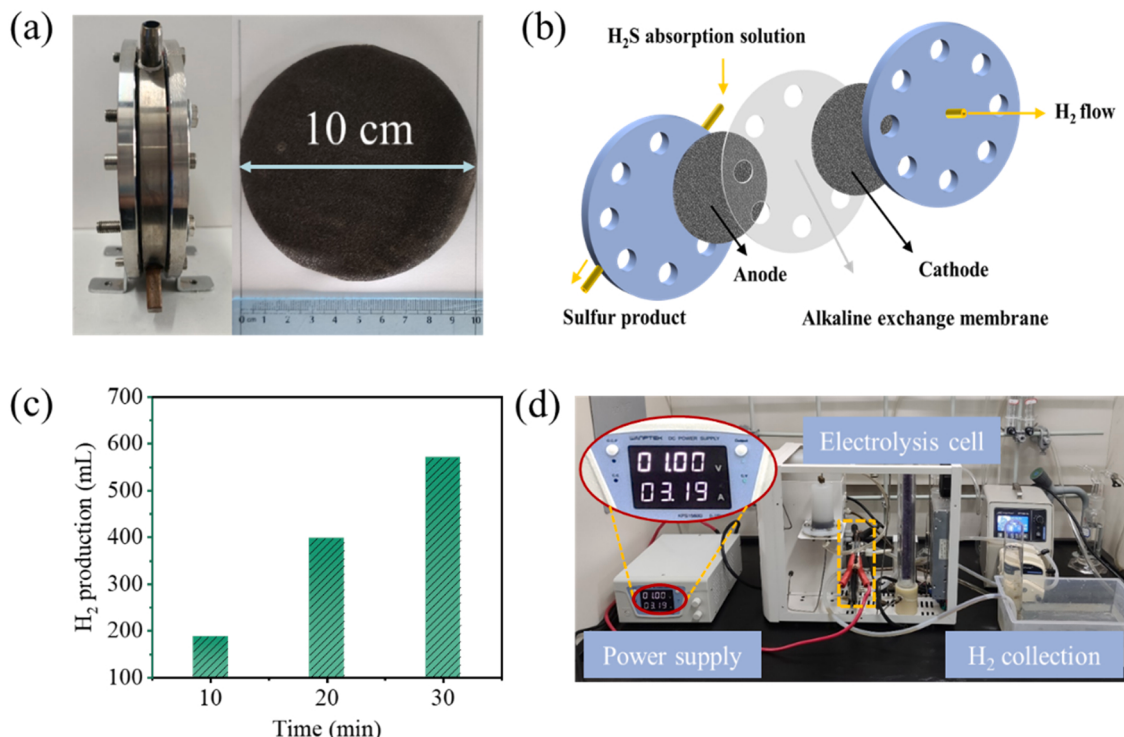


Fig. 6. (a) Photograph of an electrolyzer device and large area NiSe/NF electrode; (b) Schematic illustration of the structure of an electrolyzer cell; (c) Amount of H₂ production at 1.0 V; (d) Photograph of the electrolysis cell used in the machine testing at 1.0 V voltage.

Meanwhile, there is no signal of polysulfide because of weak signal for S-S bond vibration in ATR-FTIR. Raman spectroscopy could work well for sulfur-containing aqueous solutions. Hence, we designed *in situ* Raman spectroscopy cell to probe the sulfur oxidative products (Fig. S10b). The Raman spectra of various sulfur-related species were given in Fig. S13 as references. Table S4 shows the characteristic peaks of SO₃²⁻ (466 cm⁻¹, 612 cm⁻¹, 962 cm⁻¹), S₂O₃²⁻ (334 cm⁻¹, 443 cm⁻¹, 532 cm⁻¹, 664 cm⁻¹, 997 cm⁻¹, 1123 cm⁻¹), SO₄²⁻ (978 cm⁻¹), S (151 cm⁻¹, 216 cm⁻¹, 471 cm⁻¹), HS⁻ (2571 cm⁻¹), S_n²⁻, according to the reported work [46,47,50–55,57,58].

Fig. 5a exhibits obvious peaks with enhancement during the SOR. Among them, the Raman signal at 415 cm⁻¹, 443 cm⁻¹ are indexed to the S_n²⁻, and the Raman signal at 443 cm⁻¹, 663 cm⁻¹, and 993 cm⁻¹ are assigned to the S₂O₃²⁻. With the potential increase, the peak strength of

S_n²⁻ and S₂O₃²⁻ also increases, consistent with ATR-FTIR and UV-vis. The faradic efficiency of S₂²⁻ and S₂O₃²⁻ were 88.1 % and 2.3 % respectively after calculation (Fig. S14c-d). All these results reveal that S²⁻/HS⁻ has been mostly converted to polysulfide and by-product S₂O₃²⁻ in NaOH solution, as shown in Fig. 5b. This chain-grown mechanism of polysulfides reveals that NiSe/NF electrode is capable of continuously catalyzing polysulfides from short to long chains, which prevents NiSe/NF from sulfur passivation for efficient H₂ evolution coupling synchronous desulfurization.

3.4. Potential industrial applications

For potential industrial applications, the large area NiSe/NF was prepared (Fig. 6a). Then, the cutted NiSe/NF electrode with 6 cm

diameter was used in a commercial membrane electrode assembly stack, which consisted of one HER cell and one SOR cell (Fig. 6b). The system uses NiSe/NF as the cathode and anode catalysts. Particularly, with the cell voltage of 1.0 V, the NiSe/NF||NiSe/NF couple electrolyzer shows a 19.0 mL min^{-1} H_2 production rate with current density of 106 mA cm^{-2} as shown in Fig. 6c and d, while under such potential cannot drive water splitting with no H_2 production. Moreover, the HER coupled SOR system consumes electricity of 2.63 kWh Nm^{-3} much lower than water splitting at a low cell voltage of 1.0 V ($4.0\text{--}6.0 \text{ kWh Nm}^{-3}$) [59]. Taking all things into account, the anti-sulfuretted NiSe/NF catalyst demonstrates its potential in energy-saving electrocatalytic H_2 generation coupling the high-value utilization of H_2S .

4. Conclusions

In summary, the anti-sulfuretted NiSe/NF nanowire array has been demonstrated as a superior catalyst for efficient electrocatalytic H_2 generation coupling desulfurization. It showed around 99 % H_2 faradaic efficiency and remained 500 h stability without decay at 0.4 V. Additionally, UV-vis, *in situ* ATR-FTIR, and Raman spectroscopy suggest that $\text{S}^{2-}/\text{HS}^-$ have been mostly converting S_n^{2-} and by-product $\text{S}_2\text{O}_3^{2-}$ in NaOH solution. Importantly, NiSe/NF||NiSe/NF membrane electrode assembly stack exhibits ultra-low electricity consumption of 2.63 kWh to $1 \text{ Nm}^3 \text{ H}_2$ production. This work not only first demonstrates of NiSe nanowire array as a highly efficient anti-sulfuretted catalyst in technological devices for energy-saving electrolytic H_2 generation from H_2S splitting but also deep insights into the SOR mechanisms, further guiding the rational design of more advanced electrocatalysts.

CRediT authorship contribution statement

Chao Duan: Conceptualization, Methodology, Investigation, Writing-Original Draft. **Shan Yu:** Formal analysis, Methodology, Validation, Investigation. **Jinjin Li:** Methodology, Resources. **Lina Li:** Resources, Methodology. **Chun Tang:** Conceptualization, Supervision, Funding acquisition. **Ying Zhou:** Supervision, Conceptualization, Project administration, Funding acquisition.

Declaration of Competing Interest

The authors declare that they have no known competing financial interests or personal relationships that could have appeared to influence the work reported in this paper.

Data Availability

Data will be made available on request.

Acknowledgments

We gratefully acknowledge financial support from the National Natural Science Foundation of China (No 22178291, 22002123, 22109132), the Provincial Key Research and Development Project of Sichuan (2022YFSY0052, 2022NSFSC0023, 2021YFSY0046), Natural Science Foundation of Sichuan (2022NSFSC1264), Science Project of SWPU (2021JBGS01), Scientific research starting project of SWPU (No.2021QHZ014). We thank the staff at the BL11B beamline of Shanghai Synchrotron Radiation Facilities (SSRF) for assistance with the XAFS measurements.

Appendix A. Supporting information

Supplementary data associated with this article can be found in the online version at doi:10.1016/j.apcatb.2022.122255.

References

- [1] C.N. Zou, Z. Yang, D.B. He, Y.S. Wei, J. Li, A.L. Jia, J.J. Chen, Q. Zhao, Y.L. Li, J. Li, S. Yang, Petrol. Explor. Dev. + 45 (2018) 604–618.
- [2] M. Li, X.Q. Zheng, L. Li, Z.D. Wei, Acta Phys. Chim. Sin. 37 (2021), 2007054-2007050.
- [3] X.S. Wang, Y. Zheng, W.C. Sheng, Z.C.J. Xu, M. Jaroniec, S.Z. Qiao, Mater. Today 36 (2020) 125–138.
- [4] Z.H. Li, Y.F. Yan, S.M. Xu, H. Zhou, M. Xu, L.N. Ma, M.F. Shao, X.G. Kong, B. Wang, L.R. Zheng, H.H. Duan, Nat. Commun. 13 (2022) 1–14.
- [5] W.J. Liu, Z. Xu, D. Zhao, X.Q. Pan, H.C. Li, X. Hu, Z.Y. Fan, W.K. Wang, G.H. Zhao, S. Jin, Nat. Commun. 11 (2020) 1.
- [6] C. Tang, R. Zhang, W.B. Lu, Z. Wang, D.N. Liu, S. Hao, G. Du, A.M. Asiri, X.P. Sun, Angew. Chem. Int. Ed. 56 (2017) 842–846.
- [7] M. Dan, S. Yu, Y. Li, S.Q. Wei, J.L. Xiang, Y. Zhou, J. Photoch. Photobio. C 42 (2020), 100339.
- [8] Z.H. Xie, S. Yu, X.B. Fan, S.Q. Wei, L.M. Yu, Y.Q. Zhong, X.W. Gao, F. Wu, Y. Zhou, J. Energy Chem. 52 (2021) 234–242.
- [9] X.P. Li, C. Huang, W.K. Han, T. Ouyang, Z.Q. Liu, Chin. Chem. Lett. 32 (2021) 2597–2616.
- [10] M. Dan, S.Q. Wei, D.E. Doronkin, Y. Li, Z.Y. Zhao, S. Yu, J.D. Grunwaldt, Y.H. Lin, Y. Zhou, Appl. Catal. B-Environ. 243 (2019) 790–800.
- [11] A.G. De Crisci, A. Moniri, Y.M. Xu, Int. J. Hydrot. Energy 44 (2019) 1299–1327.
- [12] H.Y. Huang, Y. Yu, K.H. Chung, Energ. Fuel. 23 (2009) 4420–4425.
- [13] H.Y. Huang, J. Shang, Y. Yu, K.H. Chung, Int. J. Hydrot. Energy 44 (2019) 5108–5113.
- [14] W.G. Ma, H. Wang, W. Yu, X.M. Wang, Z.Q. Xu, X. Zong, C. Li, Angew. Chem. Int. Ed. 57 (2018) 3473–3477.
- [15] K. Obata, Y. Shinohara, S. Tanabe, I. Waki, K. Kotovos, K. Ohkawa, K. Takanabe, Energy Technol., Ger. 7 (2019), 1900575.
- [16] Q.W. Zhou, Z.H. Shen, C. Zhu, J.C. Li, Z.Y. Ding, P. Wang, F. Pan, Z.Y. Zhang, H. X. Ma, S.Y. Wang, H.G. Zhang, Adv. Mater. 30 (2018), 1800140.
- [17] B. Zhang, J. Bai, Y. Zhang, C.H. Zhou, P.B. Wang, L.N. Zha, J.H. Li, A. Simchi, B. X. Zhou, Environ. Sci. Technol. 55 (2021) 14854–14862.
- [18] J.L. Lee, Y.S. Shih, Ind. Eng. Chem. Process Des. Dev. 25 (1986) 834–836.
- [19] S. Alexander, J. Winnick, Sep. Sci. Technol. 25 (1990) 2057–2072.
- [20] Y.J. Ma, X.B. Jin, Y. Hu, Q. Huang, Z.Y. Wang, Energ. Fuel. 34 (2020) 7756–7762.
- [21] M. Zhang, J. Guan, Y.C. Tu, S.M. Chen, Y. Wang, S.H. Wang, L. Yu, C. Ma, D. H. Deng, X.H. Bao, Energy Environ. Sci. 13 (2020) 119–126.
- [22] M. Zhang, J. Guan, Y.C. Tu, S.H. Wang, D.H. Deng, Innovation 2 (2021), 100144.
- [23] S. Zhang, Q.W. Zhou, Z.H. Shen, X. Jin, Y.C. Zhang, M. Shi, J. Zhou, J.G. Liu, Z. D. Lu, Y.N. Zhou, H.G. Zhang, Adv. Funct. Mater. 31 (2021), 2101922.
- [24] L.C. Yi, Y.X. Ji, P. Shao, J.X. Chen, J.W. Li, H. Li, K. Chen, X.X. Peng, Z.H. Wen, Angew. Chem. Int. Ed. 60 (2021) 21550–21557.
- [25] Y.H. Pei, J. Cheng, H. Zhong, Z.F. Pi, Y. Zhao, F.M. Jin, Green. Chem. 23 (2021) 6975–6983.
- [26] M. Kumar, T.C. Nagaiah, J. Mater. Chem. A 10 (2022) 7048–7057.
- [27] L.Y. Zhang, Z.Y. Wang, J.S. Qiu, Adv. Mater. 34 (2022), 2109321.
- [28] F.E. Bedoya-Lora, A. Hankin, G.H. Kelsall, Electrochim. Acta 314 (2019) 40–48.
- [29] S. Yu, F. Wu, P.K. Zou, X.B. Fan, C. Duan, M. Dan, Z.H. Xie, Q. Zhang, F.Y. Zhang, H. Zheng, Y. Zhou, Chem. Commun. 56 (2020) 14227–14230.
- [30] I. Grigioni, M. Bernareggi, G. Sinibaldi, M.V. Dozzi, E. Sell, Appl. Catal. A- Gen. 518 (2016) 176–180.
- [31] Y. Zhong, Y. Shao, F. Ma, Y. Wu, B. Huang, X. Hao, Nano Energy 31 (2017) 84–89.
- [32] Y.L. Zhiliang Jin, Xuqiang Hao Ni, Acta Phys. Chim. Sin. 10 (2021), 1912033.
- [33] Y. Wang, X. Li, M. Zhang, Y. Zhou, D. Rao, C. Zhong, J. Zhang, X. Han, W. Hu, Y. Zhang, K. Zaghib, Y. Wang, Y. Deng, Adv. Mater. 32 (2020), e2000231.
- [34] T. Yan, J. Feng, P. Zeng, G. Zhao, L. Wang, C. Yuan, C. Cheng, Y. Li, L. Zhang, J. Energy Chem. 74 (2022) 317–323.
- [35] X. Zhang, Y.Y. Zhang, Y. Zhang, W.J. Jiang, Q.H. Zhang, Y.G. Yang, L. Gu, J.S. Hu, L.J. Wan, Small Methods 3 (2018), 1800317.
- [36] C. Tang, N.Y. Cheng, Z.H. Pu, W. Xing, X.P. Sun, Angew. Chem. Int. Ed. 54 (2015) 9351–9355.
- [37] L.W. Mi, H. Sun, Q. Ding, W.H. Chen, C.T. Liu, H.W. Hou, Z. Zheng, C.G. Shen, Dalton T. 41 (2012) 12595–12600.
- [38] S.L. Han, Y.N. Hao, Z.Y. Guo, D.S. Yu, H.J. Huang, F. Hu, L.L. Li, H.Y. Chen, S. J. Peng, Chem. Eng. J. 401 (2020), 126088.
- [39] H.Q. Zhou, F. Yu, Y.F. Huang, J.Y. Sun, Z. Zhu, R.J. Nielsen, R. He, J. Bao, W. A. Goddard, S. Chen, Z.F. Ren, Nat. Commun. 7 (2016) 12765.
- [40] R.L. Doyle, M.E.G. Lyons, J. Electrochem. Soc. 160 (2013) H142–H154.
- [41] Z.H. Xiao, Y.C. Huang, C.L. Dong, C. Xie, Z.J. Liu, S.Q. Du, W. Chen, D.F. Yan, L. Tao, Z.W. Shu, G.H. Zhang, H.G. Duan, Y.Y. Wang, Y.Q. Zou, R. Chen, S.Y. Wang, J. Am. Chem. Soc. 142 (2020) 12087–12095.
- [42] I.G.D. Lana, Q.L. Zhang, K.T. Chuang, H. Wang, Ind. Eng. Chem. Res. 39 (2000) 2505–2509.
- [43] J.P. Fornés, J.M. Bisang, Electrochim. Acta 243 (2017) 90–97.
- [44] C.A. Linkous, C. Huang, J.R. Fowler, J. Photoch. Photobio. A 168 (2004) 153–160.
- [45] J. Lee, W. Choi, J. Eletrochem. Soc. 162 (2015) A935–A939.
- [46] C. Schmid, T.M. Seward, Chem. Geol. 467 (2017) 64–75.
- [47] E.A. Nicol, J.Y. Baron, J. Mirza, J.J. Leitch, Y. Choi, J. Lipkowski, J. Solid, State Electr. 18 (2013) 1469–1484.
- [48] Y. Li, Y. Duan, K. Zhang, W. Yu, Chem. Eng. J. 433 (2022), 134472.
- [49] M. Kumar, T.C. Nagaiah, J. Mater. Chem. A 10 (2022) 13031–13041.
- [50] K.U.V. Raben, P.B. Dorain, R.K. Chang, B.L. Laube, Chem. Phys. Lett. 84 (1987) 405–409.

[51] C. Nims, B. Cron, M. Wetherington, J. Macalady, J. Cosmidis, *Sci. Rep.* 9 (2019) 7971.

[52] R.L. Aggarwal, L.W. Farrar, D.L. Polla, J. Raman, *Spectrosc.* 42 (2011) 461–464.

[53] S. Sun, T. Cai, Y. Liu, J. Wang, *J. Appl. Spectrosc.* + 82 (2015) 182–187.

[54] G. Ma, H.G. Yan, J.Y. Shi, X. Zong, Z.B. Lei, C. Li, *J. Catal.* 260 (2008) 134–140.

[55] C.L. Corkhill, P.L. Wincott, J.R. Lloyd, D.J. Vaughan, *Geochim. Cosmochim. Ac.* 72 (2008) 5616–5633.

[56] G. Kartopu, A.V. Sapelkin, V.A. Karavanskii, U. Serincan, R. Turan, *J. Appl. Phys.* 103 (2008), 113518.

[57] J.P. Lelieur, P. Dubois, G. Lepoutre, *Inorg. Chem.* 27 (1988) 1883–1890.

[58] J. Li, J.J. Lu, X.C. Lu, B. Tu, B.J. Ouyang, X.D. Han, R.C. Wang, *Geomicrobiol. J.* 33 (2016) 118–134.

[59] F. Sun, D.T. He, K.Z. Yang, J.S. Qiu, Z.Y. Wang, *Angew. Chem. Int. Ed.* 61 (2022), e202203929.